

ACOUSTICS OF STRUCTURALLY INHOMOGENEOUS SOLID BODIES. GEOLOGICAL ACOUSTICS

Surface Waves in Materials with Functionally Gradient Coatings

E. V. Glushkov^a, N. V. Glushkova^a, S. I. Fomenko^a, and C. Zhang^b

^a Kuban State University, ul. Stavropol'skaya 149, Krasnodar, 350040 Russia

^b University of Siegen, Paul-Bonatz str. 9-11, Siegen, D-57076 Germany

e-mail: evg@math.kubsu.ru

Received August 9, 2011

Abstract—Surface wave excitation and propagation in a half-space with a continuous dependence of elastic properties on depth has been considered. The total wave field generated by a given surface load can be represented as a convolution of the Green's matrix of the medium with the vector of surface stresses, while the traveling surface waves are described by the residues from the poles of the Green's matrix Fourier symbol. Comparison of the gradient and multilayer models shows that with a high enough number of partitions (layers), the dispersion properties and amplitude–frequency characteristics of surface waves in FGMs are described by the curves obtained upon a steplike approximation of gradient properties; however, with high contrast properties, the multilayer model can be more time-consuming. The effect of the vertical inhomogeneity of the medium on the surface wave characteristics has been analyzed for a series of typical dependences occurring in micro- and nanocoatings due to diffusions or technological features of sputtering and gluing of protective films.

Keywords: functionally gradient material, Green's matrix, layer-inhomogeneous medium, surface waves.

DOI: 10.1134/S1063771012010095

INTRODUCTION

At present, media with a continuous dependence of the elastic properties on the depth are usually called functionally graded materials (FGMs). The necessity of solving wave problems for FGMs occurs in hydro-, seismo-, and physical acoustics, as well as in connection with the appearance of new composite materials, film microelectronic piezoelectric structures, and materials with protective micro- and nanocoatings. The elastic properties of such materials gradually vary due to the technology of their fabrication (sputtering, sintering) or diffusion processes in the interlayer gluing of dissimilar-module layers. In some cases, it is a special task to reduce the contrast of the elastic properties of a composite (for example, metal ceramics) in order to reduce internal stresses occurring under temperature and force loads. Materials with strengthening gradient coatings are widely used; accordingly, there is an increasing need to develop reliable nondestructive wave methods for their control.

To determine the elastic properties of FGMs, indentation or ultrasonic probing data are used. The theoretical analysis of indentation results is based on solving the corresponding contact problems, while remote ultrasonic control is based on analysis of surface acoustic waves (SAWs). The purpose of this work is to simulate SAWs excited by a given surface load in open FGM waveguides.

The finite element method (FEM) and finite difference method (FDM) are universal approaches to solving the initial-boundary problems for an inhomogeneous medium. However, in the case of wave problems, this approach has known drawbacks. First, this is the sharp increase of computing expenses when the relative size of the considered region increases, which strongly hampers simulation of remote probing of lengthy structures. Second, due to absence of information on the contribution of each of the excited modes to the total wave field, physical clarity of the results is not always ensured.

Normal mode characteristics can be obtained by the modal analysis technique by searching for spectral points and corresponding eigensolutions (eigenmodes) of the homogeneous boundary value problems for the considered waveguides. However, the modal analysis does not give information on the relationship between the amplitudes of excited waves, which depends on the source parameters. This necessitates developing hybrid schemes, within which the unknown amplitude coefficients are determined by coupling normal mode expansions with the FEM/FDM near-field results [1].

An *integral approach* is more natural, not requiring such a joining. Within this approach, the total wave field (displacement field \mathbf{u}) is represented as a convolution of the Green's matrix of the considered

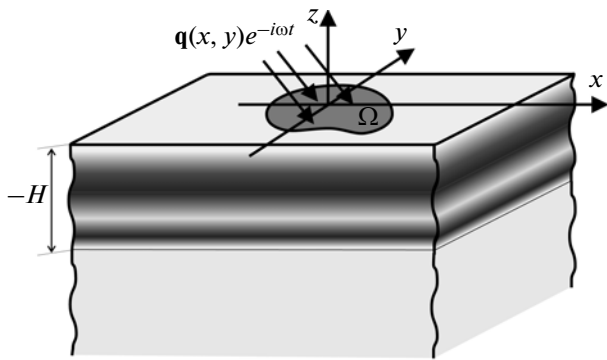


Fig. 1. Functionally graded elastic half-space with surface load.

waveguide k with the surface load vector \mathbf{q} simulating the source action [2]:

$$\mathbf{u}(\mathbf{x}) = \int_{\Omega} k(\mathbf{x} - \xi) \mathbf{q}(\xi) d\xi. \tag{1}$$

Here and below, the spatial points $\mathbf{x} = (x, y, z)$ are considered as given in the coordinate system with the origin O in the load area Ω ; the xOy plane coincides with the day surface of the medium, and the Oz axis is its outward normal (Fig. 1).

The equations and boundary conditions of the corresponding boundary value problems for stratified media whose properties are independent of the horizontal coordinates x, y , including those for the considered FGM, permits the application of Fourier transformation \mathcal{F}_{xy} over these coordinates. This allows one to write the Green’s matrix as an inverse Fourier transformation:

$$k(\mathbf{x}) = \mathcal{F}_{xy}^{-1}[K] = \frac{1}{(2\pi)^2} \int_{\Gamma_1} \int_{\Gamma_2} K(\alpha_1, \alpha_2, z) e^{-i(\alpha_1 x + \alpha_2 y)} d\alpha_1 d\alpha_2. \tag{2}$$

The wave field representation (1) is reduced to the inverse transformation from the product of the Fourier symbols of the Green’s matrix $K = \mathcal{F}_{xy}[k]$ and load $\mathbf{Q} = \mathcal{F}_{xy}[\mathbf{q}]$: $\mathbf{u} = \mathcal{F}_{xy}^{-1}[K\mathbf{Q}]$. The replacement of the contour integrals by the sum of the residues of the elements of the matrix $K(\alpha_1, \alpha_2, z)$ from the poles ζ_n gives the expansion of $\mathbf{u}(\mathbf{x})$ in terms of normal modes. The residues, being functions of z , give the same depth dependences of the SAW components as does the modal analysis, while the information on the source automatically enters the amplitude coefficients via the \mathbf{Q} values at the poles ζ_n . Construction of the K matrix and the search for the real and close-to-real axis poles of its element is of key importance for implementing this approach.

In the 1970s–1980s, the integral approach was performed for multilayer and gradient media for which it

is difficult or impossible to write the matrix K explicitly. Methods for solving such problems arising in geophysics and seismoacoustics were actively being developed at that time at the Research Institute for Mechanics and Applied Mathematics of Rostov State University [3–6]. Providing high speed and numerical stability of algorithms for calculating the K matrix for the entire range of input parameters is of special importance for their implementation. In particular, there have been proposed and implemented the algorithms for Green’s matrix calculations, the efficiency of which was ensured by taking the exponential components out of the computing process [7]. The algorithms developing this approach are used in this work.

The calculation of the K matrix for FGM is generally more costly than for a medium with a piecewise-constant depth dependence of the properties. The approach based on the replacement of FGMs by a multilayer half-space dates back to the first matrix Thompson–Haskell–Petrashen’ algorithms [8–10], but its appropriateness remains open to question. Its ambiguity is indicated, for example, when the structures of the contact problem solutions obtained for gradient and steplike elastic bases are compared [5]. The behavior of the Fourier symbol of the kernel of the integral equation at infinity in these two cases is qualitatively different. In certain situations this leads to an invalid interpretation of indentation results for samples with FGM coatings.

On the other hand, there are no examples where, with a sufficient number of partitions, the steplike approximation would lead to qualitatively invalid wave characteristics recorded on the surface of FGM waveguides. On the contrary, the known numerical results (see, e.g., [11]) allow one to suppose that it is possible to use a low-cost multilayer model for simulating SAWs in FGM waveguides. One of the aims of this work is to check this suggestion, based on a systematic comparison of the results obtained by means of the algorithms elaborated for fast calculation of Green’s matrices for elastic half-spaces with gradient and piecewise-constant depth dependences. The formulation and description of the general scheme of the solution to the corresponding problems and the algorithms used for K matrix calculation are preliminarily given. Then, for a series of typical dependences occurring in materials with coatings and layered composites, numerical results are given and discussed that show the dependence of the discrepancy on the number of partitions when the FGM model is replaced with the multilayered one. Of independent interest are the results showing the effect of inhomogeneity on the dispersion and amplitude–frequency characteristics of SAWs excited by a given surface source, as well as typical features of the motion of the K matrix poles (spectral points determining the normal modes) in the complex plane.

INTEGRAL AND ASYMPTOTIC REPRESENTATIONS OF THE WAVE FIELD

An elastic isotropic half-space occupying the volume $-\infty < x, y < \infty$, $-\infty < z \leq 0$ in the Cartesian coordinate system is considered. The elastic modules λ and μ and the density ρ continuously vary with the depth z , reaching constant values at $z < -H$ (Figs. 1 and 2). Such a dependence simulates materials with a functionally graded coating of thickness H .

The steady-state time-harmonic oscillation of the medium $\mathbf{u}(\mathbf{x})e^{-i\omega t}$ with the circular frequency ω are excited by the load $\mathbf{q}e^{-i\omega t}$ applied to the stress-free surface $z = 0$ in a restricted area Ω :

$$\boldsymbol{\tau}|_{z=0} = \begin{cases} \mathbf{q}(x, y), & (x, y) \in \Omega, \\ 0, & (x, y) \notin \Omega, \end{cases} \quad (3)$$

$\boldsymbol{\tau} = \{\tau_{xz}, \tau_{yz}, \sigma_z\} = \{\tau_1, \tau_2, \tau_3\}$ is the complex amplitude of a stress vector on a horizontal surface. At infinity $z \rightarrow -\infty$ and $r = \sqrt{x^2 + y^2} \rightarrow \infty$, the radiation conditions resulting from the principle of limiting absorption hold [2]. Here and below, the time-harmonic factor $e^{-i\omega t}$ is omitted, and in addition to conventional notations, digital indexing of the vector and matrix components is used, which is necessary for compact tensor records with summation over identical indices. The vector–column components are given in braces.

The displacement vector $\mathbf{u} = \{u_x, u_y, u_z\} = \{u_1, u_2, u_3\}$ obeys the equations of motion

$$\sigma_{ij,j} + \rho\omega^2 u_i = 0, \quad (4)$$

in which the derivatives of the components u_i enter via the stress tensor elements,

$$\sigma_{ij} = \lambda \operatorname{div} \mathbf{u} + \mu (u_{i,j} + u_{j,i}), \quad i, j = 1, 2, 3. \quad (5)$$

The substitution of Eq. (5) into Eq. (4) leads to the system of equations

$$(\lambda + \mu) \nabla \operatorname{div} \mathbf{u} + \mu \Delta \mathbf{u} + \rho\omega^2 \mathbf{u} + \mathbf{D}(\mathbf{u}) = 0, \quad (6)$$

which differs from the Lamé equations for a homogeneous medium by the additional term \mathbf{D} , containing derivatives of the elastic modules $\lambda(z)$ and $\mu(z)$ depending on $z = x_3$:

$$\mathbf{D} = \{\mu'(u_{1,3} + u_{3,1}), \mu'(u_{2,3} + u_{3,2}), \lambda' \operatorname{div} \mathbf{u} + 2\mu' u_{3,3}\}.$$

In the case of piecewise-continuous dependence of λ and μ on z with the points of discontinuity $z = z_m$, Eqs. (6) are determined in the open regions (sublayers) S_m : $z_{m+1} < z < z_m$ ($m = 1, 2, \dots, M$, $z_1 = 0$, $z_{M+1} = -\infty$), and the additional conditions of the displacement and stress continuity are assigned on their boundaries:

$$[\mathbf{u}]_m = 0, \quad [\boldsymbol{\tau}]_m = 0, \quad m = 2, 3, \dots, M. \quad (7)$$

Square brackets denote the jumps of the corresponding functions at the boundaries $z = z_m$: $[\mathbf{u}]_m = \lim_{\varepsilon \rightarrow 0} (\mathbf{u}|_{z_m - \varepsilon} - \mathbf{u}|_{z_m + \varepsilon})$. For a layered-homogeneous medium, Eqs. (6) degenerate into the classical Lamé

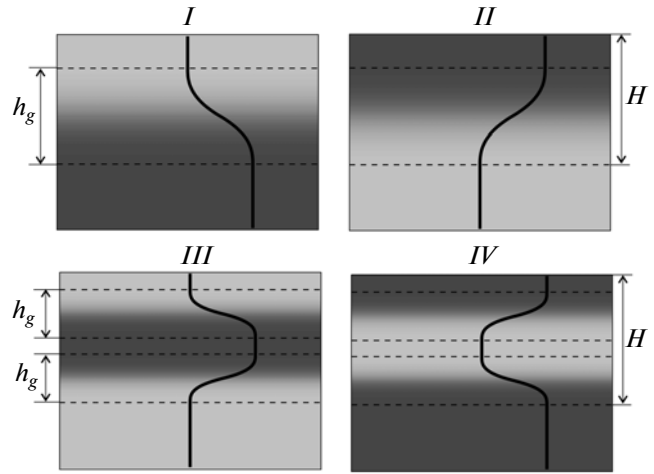


Fig. 2. Four types of gradient coatings.

equations with $\mathbf{D} \equiv 0$ and constant coefficients $\lambda = \lambda_m$, $\mu = \mu_m$ and $\rho = \rho_m$ within every sublayer S_m .

Remark. In some works (see, e.g., [6, 11]), the Green's matrix for an FGM is calculated by numerically solving the initial first-order Eqs. (4) and (5) in the Fourier transform domain, not reducing them to Eq. (6). It has been stated that, thus, it is possible to avoid differentiation of the elastic moduli λ , μ and discard problems resulting from the presence of discontinuity points z_m . However, this difference is apparent: with any method for numerically solving the arising systems of ordinary differential equations (ODEs), the finite-difference schemes are equivalent, since differentiation of λ and μ over z is implicitly present in relations (4) and (5) and the discontinuity points in both cases are passed using the coupling conditions (7).

The columns \mathbf{k}_j of the matrix $\mathbf{k} = (\mathbf{k}_1, \mathbf{k}_2, \mathbf{k}_3)$ in Eq. (1) are the displacement vectors caused in the considered medium by the point loads,

$$\boldsymbol{\tau}|_{z=0} = \delta(x, y) \mathbf{i}_j, \quad j = 1, 2, 3, \quad (8)$$

applied to its surfaces along the coordinate axes Ox_j ; δ is the Dirac delta function and \mathbf{i}_j are the coordinate unit vectors. In conventional notations [2, 12], the Fourier symbol $K(\alpha_1, \alpha_2, z)$ is expressed in terms of five functions M , N , P , R , and S , depending only on $\alpha = \sqrt{\alpha_1^2 + \alpha_2^2}$ and z :

$$K = \begin{pmatrix} -i(\alpha_1^2 M + \alpha_2^2 N) & -i\alpha_1 \alpha_2 (M - N) & -i\alpha_1 P \\ -i\alpha_1 \alpha_2 (M - N) & -i(\alpha_1^2 N + \alpha_2^2 M) & -i\alpha_2 P \\ \alpha_1 S & \alpha_2 S & R \end{pmatrix}. \quad (9)$$

In cylindrical (polar) coordinates,

$$x = r \cos \varphi, \quad y = r \sin \varphi, \quad r = \sqrt{x^2 + y^2} \\ \alpha_1 = \alpha \cos \gamma, \quad \alpha_2 = \alpha \sin \gamma, \quad \alpha = \sqrt{\alpha_1^2 + \alpha_2^2},$$

the matrix $K_c = C^{-1}(\gamma)KC(\gamma)$ connecting the Fourier symbols of the load vectors $\mathbf{q}_c = \{q_r, q_\varphi, q_z\}$ and of the displacements $\mathbf{u}_c = \{u_r, u_\varphi, u_z\}$: $\mathbf{U}_c = K_c\mathbf{Q}_c$, has the form

$$K_c(\alpha, z) = \begin{pmatrix} -i\alpha^2 M & 0 & -i\alpha P \\ 0 & -i\alpha^2 N & 0 \\ iS & 0 & R \end{pmatrix}, \quad (10)$$

$$C(\gamma) = \begin{pmatrix} \cos \gamma & -\sin \gamma & 0 \\ \sin \gamma & \cos \gamma & 0 \\ 0 & 0 & 1 \end{pmatrix}.$$

Its structure indicates that the displacements u_r and u_z in the radial plane (r, φ) and the torsion oscillation u_φ are caused independently by the stress components q_r, q_z , and q_φ . In outward appearance, the same structure is obtained for the matrix K in the plane case, when \mathbf{u} and \mathbf{q} do not depend on the transverse coordinate y . In such a case, the integral in Eq. (2) is a single one, $\alpha_2 = 0$, $\alpha = \alpha_1$, and the function $N(\alpha, z)$ in the K_{22} component is in charge of the antiplane oscillations generated by the load $\tau_{yz} = q_2(x, z)$.

The change of variables to polar coordinates allows one to reduce Eq. (2) to a single integral over α and, in turn, to a series in terms of residues in the N_r real and infinite number of complex poles ζ_n of these functions (contribution of the discrete spectrum) plus the remaining integrals over the banks of cuts (contribution of the continuous spectrum), giving the term k_b [12, 15]:

$$k(\mathbf{x}) = \sum_{n=1}^{\infty} k_n(\mathbf{x}) + k_b(\mathbf{x}), \quad (11)$$

$$k_n(\mathbf{x}) = \sum_{p=-2}^2 R_{np}(z) H_p^{(1)}(\zeta_n r) e^{-ip(\varphi+\pi/2)},$$

$$R_{np} = \frac{i}{2} j_n \zeta_n \text{res} K_p(\alpha, z) |_{\alpha=\zeta_n},$$

$$K_p : K(\alpha, \gamma, z) = \sum_{p=-2}^2 K_p(\alpha, z) e^{-ip\gamma},$$

where $H_p^{(1)}$ are Hankel functions, $j_n = -1$, if ζ_n is an irregular real pole, giving the backward wave; for the rest of the poles, $j_n = 1$.

Due to the asymptotic behavior of the Hankel functions for large arguments, the terms $k_n(\mathbf{x})$ corresponding to the complex ζ_n (inhomogeneous waves) exponentially decay as r increases, while, taking into

account Eq. (1), the real poles give the far-field asymptotics [12]:

$$\mathbf{u}(\mathbf{x}) = \sum_{n=1}^{N_r} \mathbf{u}_n(\mathbf{x}) \left[1 + O((\zeta_n r)^{-1}) \right], \quad (12)$$

$$\zeta_n r \rightarrow \infty, \quad \dim \Omega / r \ll 1,$$

$$\mathbf{u}_n(\mathbf{x}) = \mathbf{b}_n(\varphi, z) e^{i\zeta_n r} / \sqrt{\zeta_n r},$$

$$\mathbf{b}_n = \sqrt{\frac{i}{2\pi}} \zeta_n \text{res} K(\alpha, \varphi, z) |_{\alpha=\zeta_n} \mathbf{Q}(-\zeta_n, \varphi).$$

The terms of Eq. (12) describe the traveling waves of the Rayleigh–Lamb–Stoneley type (for the poles ζ_n of functions M, P, R , and S) and antiplane Love waves (for the poles of functions N) propagating in the FGM half-space from the area of the application of the load \mathbf{q} with the phase and group velocities $v_n = \omega/\zeta_n$ and $c_n = d\omega/d\zeta_n$, respectively. The numerical examples below are given with respect to the inverse to v_n slownesses $s_n = \zeta_n/\omega$, which are poles in the complex plane $s = \alpha/\omega$.

The main contribution to the asymptotics of the entering into $k_b(\mathbf{x})$ integrals over the banks of cuts is given by the real branch points $\kappa_1 = \omega/v_p$ and $\kappa_2 = \omega/v_s$, which are the wavenumbers of body waves propagating in the lower (homogeneous) half-space $z < -H$ with the phase velocities v_p and v_s [12].

ALGORITHMS FOR CALCULATING MATRIX K

The Fourier transformation \mathcal{F}_{xy} reduces the boundary value problem for Eqs. (3), (6), and (7) to the problem for a system of ODEs over z with respect to the Fourier symbol $\mathbf{U} = \mathcal{F}_{xy}[\mathbf{u}]$. Then, by means of the substitution

$$\mathbf{U} = \begin{pmatrix} -i\alpha_1 & -i\alpha_2 & 0 \\ -i\alpha_2 & i\alpha_1 & 0 \\ 0 & 0 & 1 \end{pmatrix} \begin{pmatrix} \Phi \\ \Psi \\ W \end{pmatrix}$$

it is reduced to three independent problems with respect to the vector functions $\mathbf{Y}(\alpha, z) = \{\Phi, \Phi', W, W'\}$ and $\mathbf{X}(\alpha, z) = \{\Psi, \Psi'\}$. Specifically, these are vector functions $\mathbf{Y}_1 = \{P, P', R, R'\}$, $\mathbf{Y}_2 = \{M, M', S, S'\}$ and $\mathbf{X} = \{N, N'\}$. Their components are the functions entering the matrix K of form (9) and their z derivatives. They satisfy the ODE systems [2, 12]

$$\mathbf{Y}'_l = A(\alpha, z)\mathbf{Y}_l, \quad l = 1, 2; \quad \mathbf{X}' = B(\alpha, z)\mathbf{X} \quad (13)$$

with the boundary condition on the surface

$$T\mathbf{Y}_l |_{z=0} = \mathbf{e}_l, \quad l = 1, 2; \quad (\mathbf{l}, \mathbf{X}) = 1 \quad (14)$$

and the continuity conditions at the interfaces

$$[G\mathbf{Y}_l]_m = 0, \quad l = 1, 2; \quad [H\mathbf{X}_l]_m = 0, \quad m = 2, 3, \dots, M. \quad (15)$$

The nonzero elements of the matrices A and B in Eqs. (13) are

$$\begin{aligned} a_{12} = a_{34} = b_{12} = 1, \quad a_{41} = \alpha^2 \lambda' / (\lambda + 2\mu), \\ a_{21} = \left[\alpha^2 (\lambda + 2\mu) - \rho \omega^2 \right] / \mu, \quad a_{42} = \alpha_2 (\lambda + \mu) / (\lambda + 2\mu), \\ a_{22} = a_{23} = -\mu' / \mu, \quad a_{43} = (\alpha^2 \mu - \rho \omega^2) / (\lambda + 2\mu), \\ a_{24} = -(\lambda + \mu) / \mu, \quad a_{44} = -(\lambda' + 2\mu') / (\lambda + 2\mu), \\ b_{21} = (\alpha^2 \mu - \rho \omega^2) / \mu, \quad b_{22} = \mu' / \mu. \end{aligned}$$

The matrices and vectors in Eqs. (14) and (15) are

$$\begin{aligned} T = \begin{pmatrix} -\lambda \alpha^2 & 0 & 0 & \lambda + 2\mu \\ 0 & -i\mu \alpha^2 & -i\mu \alpha^2 & 0 \end{pmatrix}, \quad H = \begin{pmatrix} 1 & 0 \\ 0 & -i\mu \end{pmatrix}, \\ G = \begin{pmatrix} 1 & 0 & 0 & 0 \\ 0 & 0 & 1 & 0 \\ T \end{pmatrix}, \quad \mathbf{I} = (0, -i\mu \alpha^2), \quad \mathbf{e}_1 = \begin{pmatrix} 1 \\ 0 \end{pmatrix}, \quad \mathbf{e}_2 = \begin{pmatrix} 0 \\ 1 \end{pmatrix}. \end{aligned}$$

With a steplike depth dependence of the medium properties, the general solution to Eqs. (13) within every homogeneous sublayer S_m can be written in the explicit form

$$\begin{aligned} \mathbf{Y} = \sum_{j=1}^2 \left[t_m^{(j)} \mathbf{m}_j e^{\sigma_j(z-z_m)} + t_m^{(j+2)} \mathbf{m}_{j+2} e^{-\sigma_j(z-z_{m+1})} \right], \\ \mathbf{X} = s_m^{(1)} \mathbf{n}_1 e^{\sigma_2(z-z_m)} + s_m^{(2)} \mathbf{n}_2 e^{-\sigma_2(z-z_{m+1})}, \\ z \in S_m, \quad m = 1, 2, \dots, M. \end{aligned} \quad (16)$$

Here, \mathbf{m}_i and \mathbf{n}_l are the eigenvectors of the matrices of the systems corresponding to the eigenvalues $\gamma_i = \pm \sigma_j$ and $\delta_l = \pm \sigma_2$:

$$\begin{aligned} \det(A - \gamma_i I) = 0, \quad (A - \gamma_i I) \mathbf{m}_i = 0, \quad i = 1, \dots, 4, \\ \det(B - \delta_l I) = 0, \quad (B - \delta_l I) \mathbf{n}_l = 0, \quad l = 1, 2, \end{aligned}$$

where I represents the fourth-order (for \mathbf{m}_j) or second-order (for \mathbf{n}_l) unity matrices,

$$\begin{aligned} \mathbf{m}_i = \{1, \gamma_i, \gamma_i, \gamma_i^2\}, \quad i = 1, 3, \\ \mathbf{m}_i = \{\gamma_i, \gamma_i^2, \alpha^2, \alpha^2 \gamma_i\}, \quad i = 2, 4, \\ \mathbf{n}_1 = \{1, \sigma_2\}, \quad \mathbf{n}_2 = \{1, -\sigma_2\}, \\ \gamma_j = \sigma_j, \quad \gamma_{j+2} = -\sigma_j, \quad \delta_1 = \sigma_2, \quad \delta_2 = -\sigma_2, \\ \sigma_j = \sqrt{\alpha^2 - \kappa_j^2}, \quad \text{Re } \sigma_j \geq 0, \quad \text{Im } \sigma_j \leq 0, \quad j = 1, 2, \\ \kappa_1^2 = \rho \omega^2 / (\lambda + 2\mu), \quad \kappa_2^2 = \rho \omega^2 / \mu. \end{aligned}$$

The unknown coefficients $t_m^{(i)}$ and $s_m^{(i)}$ assembled in the vectors $\mathbf{t}_m = \{t_m^{(1)}, \dots, t_m^{(4)}\}$ and $\mathbf{s}_m = \{s_m^{(1)}, s_m^{(2)}\}$ are determined from the linear algebraic systems arising upon substitution of Eq. (16) into boundary conditions (14) and (15):

$$\begin{aligned} A\mathbf{t} = \mathbf{f}_l, \quad B\mathbf{s} = \mathbf{g} \\ \mathbf{t} = \{\mathbf{t}_1, \mathbf{t}_2, \dots, \mathbf{t}_M\}, \quad \mathbf{s} = \{\mathbf{s}_1, \mathbf{s}_2, \dots, \mathbf{s}_M\} \\ \mathbf{f}_l = \{\mathbf{e}_l, 0, \dots, 0\}, \quad l = 1, 2, \quad \mathbf{g} = \{1, 0, \dots, 0\}. \end{aligned} \quad (17)$$

The matrices A and B of Eqs. (17) have a block structure, allowing one to organize their solution by a matrix sweep method. The peculiarities of its implementation, providing numerical stability, are discussed further by using the first of these systems as an example.

By means of the fourth-order matrices,

$$\begin{aligned} M_m = [\mathbf{m}_1, \dots, \mathbf{m}_4] \quad \text{and} \quad E_m(z) = \text{diag}[e_1(z), \dots, e_4(z)], \\ e_j(z) = e^{\sigma_j(z-z_m)}, \quad e_{j+2}(z) = e^{-\sigma_j(z-z_{m+1})}, \quad j = 1, 2 \end{aligned}$$

the vector $\mathbf{Y}(\alpha, z)$ can be written as follows:

$$\mathbf{Y} = M_m E_m(z) \mathbf{t}_m, \quad z \in S_m.$$

The shift of parameters in the exponents $e_i(z)$ is chosen so that the first two of them ($i = 1, 2$) become unity at the upper layer boundary $z = z_m$ and the second pair ($i = 3, 4$) at the lower one $z = z_{m+1}$:

$$\begin{aligned} E_m(z_m) = \text{diag}[1, 1, e_m^{(1)}, e_m^{(2)}], \\ E_m(z_{m+1}) = \text{diag}[e_m^{(1)}, e_m^{(2)}, 1, 1], \end{aligned} \quad (18)$$

$$e_m^{(j)} = e^{-\sigma_j h_m}, \quad j = 1, 2; \quad h_m = z_m - z_{m+1}.$$

In the lower half-space ($m = M$), it is necessary to exclude exponents $e_3(z)$ and $e_4(z)$ not satisfying the radiation conditions. To this end, it is sufficient to take $t_M^{(3)} = t_M^{(4)} = 0$ and reduce the dimension of the matrix $M_m E_m$ to 4×2 .

In the matrix notation, Eqs. (14) and (15) are

$$S\mathbf{t}_l = \mathbf{e}_l, \quad l = 1, 2, \quad (19)$$

$$C_m^- \mathbf{t}_m = C_{m+1}^+ \mathbf{t}_{m+1}, \quad m = 1, 2, \dots, M-1,$$

where $S = T_1 M_1 E_1(0)$, $C_m^- = G_m M_m E_m(z_{m+1})$, and $C_m^+ = G_m M_m E_m(z_m)$. The relations

$$\mathbf{t}_m = D_m \mathbf{t}_{m+1}, \quad D_m = (C_m^-)^{-1} C_{m+1}^+, \quad m = M-1, \dots, 1 \quad (20)$$

provide the inverse run, relating \mathbf{t}_1 to \mathbf{t}_M ,

$$\mathbf{t}_1 = D \mathbf{t}_M, \quad D = D_1 D_2 \dots D_{M-1},$$

and leading to the system with respect to $\mathbf{t}_M = \{t_M^{(1)}, t_M^{(2)}\}$:

$$SD\mathbf{t}_M = \mathbf{e}_l, \quad l = 1, 2. \quad (21)$$

The remaining vectors \mathbf{t}_m are recurrently determined by means of relations (20).

In fact, this is one of the variants of the widely known transfer matrix approach (see, e.g., [13]). It requires considerably less expenditure than solving Eq. (17) as a whole, and, therefore, it is used in different modifications by many authors. However, in practice, when α increases, this algorithm fails, since the exponents $e_m^{(j)} \rightarrow 0$ at $\alpha h_m \rightarrow \infty$, which leads to rapid degeneration of the matrices C_m^- . However, the solution to system (17) as a whole remains numerically stable, since the two last and two first columns of the matrices C_m^- and C_{m+1}^+ do not contain the exponential

multipliers forming nondegenerating diagonal blocks in the matrix A . Therefore, in order to elaborate a recurrent matrix algorithm not requiring the inversion of ill-conditioned matrices, the matrix A should be split into fourth-order blocks A_{mn} : $A = [A_{mn}]_{m,n=1}^M$. The diagonal blocks A_{mm} do not contain exponents, and, due to the linear independence of the eigenvectors \mathbf{m}_j forming them, are nondegenerate matrices.

In this notation, relations (19) are

$$\begin{aligned} A_{11}\mathbf{t}_1 + A_{12}\mathbf{t}_2 &= \mathbf{f}_l, \quad \mathbf{f}_l = \{\mathbf{e}_l, 0, 0\}, \quad l = 1, 2, \\ A_{mm-1}\mathbf{t}_{m-1} + A_{mm}\mathbf{t}_m + A_{mm+1}\mathbf{t}_{m+1} &= 0, \\ m &= 2, 3, \dots, M - 1, \\ A_{MM-1}\mathbf{t}_{M-1} + A_{MM}\mathbf{t}_M &= 0, \end{aligned} \tag{22}$$

They allow one to perform a numerically stable matrix sweep according to the following scheme:

$$\begin{aligned} B_{M-1} &= -A_{MM}^{-1}A_{MM-1}, \\ B_{m-1} &= -(A_{mm} + A_{mm+1}B_m)^{-1}A_{mm-1} = 0, \\ m &= M - 1, \dots, 2, \\ B &= A_{11} + A_{12}B_1, \quad \mathbf{t}_1 = B^{-1}\mathbf{f}_l, \quad l = 1, 2, \\ \mathbf{t}_m &= B_{m-1}\mathbf{t}_{m-1}, \quad m = 2, 3, \dots, M. \end{aligned} \tag{23}$$

It should be noted that analogous methods of wave field analysis based on the explicit integral and asymptotic representations of form (11) and (12) and on the fast algorithms for calculating matrix K , have also been elaborated and computer-implemented for layered porous water-saturated media [14] and for composite materials with arbitrarily anisotropic layers [15].

In the case of FGMs, the general solution to Eqs. (13) can be written in the explicit form only for some particular dependences of properties on z ,—for example, for exponential ones. Therefore, transfer of the boundary conditions from one boundary of every layer S_m to another, which is necessary for execution of the matrix sweep algorithm, is generally possible only via numerical solution of the corresponding Cauchy problems for the ODE systems with variable coefficients. Standard finite-difference discretization (e.g., the Runge–Kutta method) leads to a numerically unstable algorithm due to the fact that, in the vicinity of the internal points $z \in S_m$, the sought solution $\mathbf{Y}(z)$ implicitly contains exponential components $e_i(z)$, giving a fast increase, degeneration to zero, or strong oscillation.

These difficulties are overcome by means of the modulating function method [7], within which the solution in each sublayer S_m is sought in the form

$$\mathbf{Y} = \sum_{j=1}^2 \left[t_m^{(j)} \mathbf{a}_j(z) e^{\gamma_j(z-z_m)} + t_m^{(j+2)} \mathbf{a}_{j+2}(z) e^{\gamma_{j+2}(z-z_{m+1})} \right] \tag{24}$$

with the unknown modulating functions $\mathbf{a}_i(z)$. The latter are determined from the Cauchy problems for the systems

$$\mathbf{a}'_i = (A(z) - \gamma_i I) \mathbf{a}_i, \quad i = 1, \dots, 4 \tag{25}$$

with the initial conditions $\mathbf{a}_i|_{z=z_0} = \mathbf{m}_i$ taken at the upper ($z_0 = z_m, i = 1, 2$) or lower ($z_0 = z_{m+1}, i = 3, 4$) boundaries of the sublayer. The eigenvalues γ_i are taken at the same initial points z_0 . At these points, the right-hand side of Eqs. (25) is zero, slowly deviating from it in the course of numerical integration over the length $z_{m+1} < z < z_m$ (the zones of drastic change in gradient properties should be divided into sublayers S_m with a sufficiently small step h_m). The vectors $\mathbf{a}_i(z)$ also change smoothly, and so the solution of ODE is low-cost and numerically stable. The algorithm for determining the unknown coefficients \mathbf{t}_m remains the same, with the obvious modification of the form of the matrices S and C_m^\pm , which are now expressed not in terms of vectors \mathbf{m}_j , but in terms of $\mathbf{a}_j(z)$, taken at boundary points $z = z_m$ and $z = z_{m+1}$.

COMPARISON OF MULTILAYER AND GRADIENT MODELS

The reliability of the results was controlled by numerically checking if the obtained solutions $\mathbf{u}(\mathbf{x})$ satisfy the equations, boundary conditions, and the energy conservation law. In addition, they were compared with the results of other authors: in particular, the same characteristics were obtained for media with an internal gradient layer like those given in monograph [6].

Four types of gradient coatings were chosen for numerical analysis: *I*, soft; *II*, hard; *III*, soft with a hard interface layer; and *IV*, hard with a soft interface (Fig. 2). Each of the coatings consists of homogeneous and gradient substrata, the latter of thickness h_g . The continuous depth dependence of properties can be given by any smooth functions relating the values of the body wave velocities $v_p = \sqrt{(\lambda + 2\mu)/\rho}$ and $v_s = \sqrt{\mu/\rho}$ and density ρ of the neighboring homogeneous substrata. Cubic splines ensuring the continuity of functions and their first derivatives were used in the calculations. At $h_g = 0$, the gradient model degenerates into a two-layer (for coatings *I* and *II*) or three-layer (for *III* and *IV*) half-space with the constant values λ_m, μ_m and ρ_m within each layer; at $h_g = H$, the coating is gradient over the total thickness. The contrast of the properties of the coatings *I* and *II* in comparison with the substrate is characterized by the ratios $\gamma_p = v_{p1}/v_{p2}, \gamma_s = v_{s1}/v_{s2}$, and $\gamma_\rho = \rho_1/\rho_2$, where the index 1 denotes values at $z = 0$ and the index 2 at $z \leq -H$.

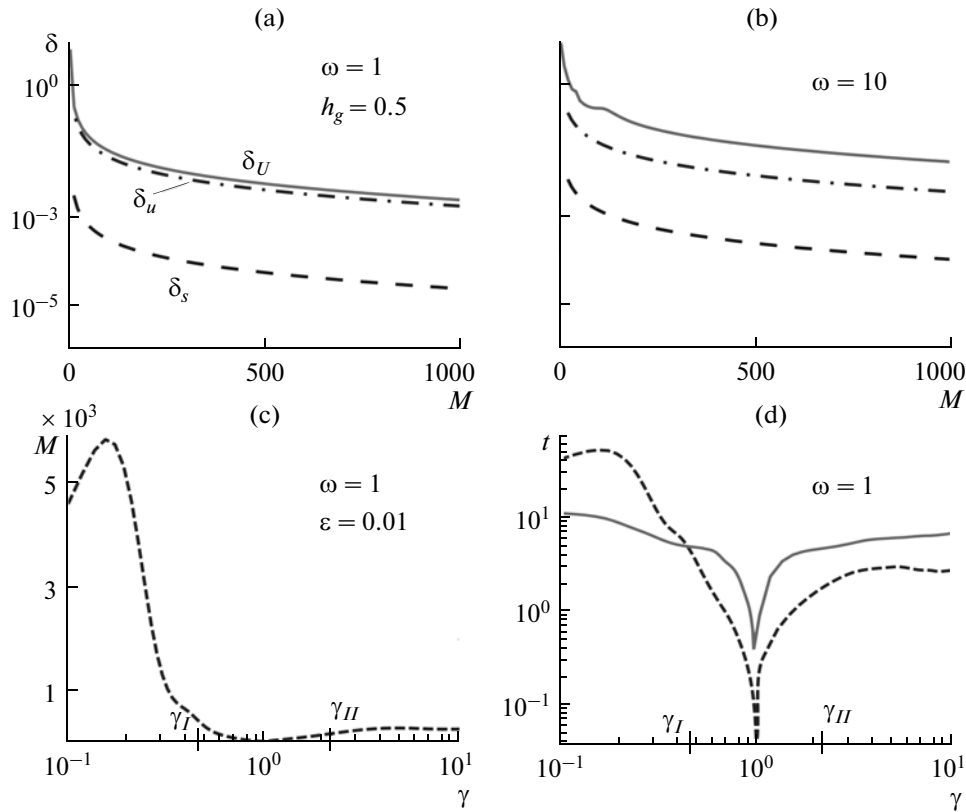


Fig. 3. Dependence of the discrepancy δ on the number of the layers M upon approximation of the continuous dependence by the steplike (a and b), as well as the number of the layers M required for achieving the given accuracy $\epsilon = 0.01$ (c) and computing costs (d) on the contrast of the elastic properties γ .

From here on, all results are given in dimensionless form, in which the linear sizes are normalized to the thickness H and the velocities and density to v_s and ρ for the hard material. In these units, the dimensionless circular frequency $\omega = 2\pi fH/v_s$, where f is dimensional frequency. For definiteness, in the numerical examples, the dimensionless parameters $v_p = 0.955$, $v_s = 0.466$, and $\rho = 0.682$ are set for the soft material, while; are normalized to the $v_p = 1.691$, $v_s = 1$, and $\rho = 1$ are for the hard one. With the velocity and density units $v_0 = 6349$ m/s and $\rho_0 = 3960$ kg/m³, these parameters correspond to the properties of aluminum (Al) and aluminium oxide (Al₂O₃). Frequencies of up to 300 kHz correspond to the dimensionless range $0 < \omega < 20$ for the thickness of the coating $H = 1$ mm. When the characteristic velocities and lengths change, the dimensional frequency range is changed as well; i.e., the results are applicable not only to micro-, but also to the corresponding macro- or nanostructures.

For comparison, M -layer media resulted from the approximation of continuous dependences by steplike functions with a uniform step were also considered. The difference between the obtained results was estimated by means of the relative integral discrepancy

$$\delta_U = \int_0^\infty \frac{\|\mathbf{U}(\alpha) - \mathbf{U}_M(\alpha)\|}{\|\mathbf{U}(\alpha)\|} d\alpha,$$

where \mathbf{U} and \mathbf{U}_M are the Fourier symbols of the displacements in the gradient and the corresponding M -layer half-space and $\|\mathbf{U}\|$ is the Euclidean norm of the vector. The discrepancies for the dispersion curves s_n and the mode amplitudes \mathbf{u}_n were analyzed as well.

Figures 3a and 3b give dependences $\delta(M)$ for the discrepancies δ_U , as well as δ_u for the sum of the amplitudes of all normal modes \mathbf{u}_n and δ_s for the maximum relative error of the slowness s_n at $\omega = 1$ and $\omega = 20$ (medium *I*). Here, just as in all the other examples considered, the discrepancies monotonically tend to zero as M increases; i.e., no cases were found for which the SAW characteristics in FGM could not be approximated with the required accuracy ϵ at a sufficiently large number of layers. The difference from the conclusions drawn in [5] is explained by the fact that the SAW characteristics are determined by the residues from limited α , while the indentation results are affected by the second expansion term of the contact problem solution which is dependent on the second term of the $K(\alpha)$ behavior at $\alpha \rightarrow \infty$, that, on the con-

trary, is qualitatively different for the gradient and multilayer media.

The number of layers M required for the achievement of accuracy $\delta_U < \varepsilon = 0.01$ versus the contrast of properties of the coatings I and II at $h_g = 0.5$, $\omega = 1$ is shown in Fig. 3c. The results are given versus $\gamma = \gamma_s$. At $\gamma < 1$ v_{s1} varies, while $v_{s2} = 1$; at $\gamma > 1$, on the contrary, $v_{s1} = 1$, while v_{s2} decreases with the increase of γ . The values of v_{p1} and ρ_1 at $\gamma < 1$ and v_{p1} and ρ_2 at $\gamma > 1$ vary similarly, so, at $\gamma = \gamma_I = 0.466$ and $\gamma = \gamma_{II} = 1/\gamma_I$, respectively, the coatings I and II with the parameters specified above occur. At $\gamma = 1$, the medium degenerates into a homogeneous half-space with the hard material properties.

The sharp increase in M at $\gamma < 1$ indicates that in this case the approximation of the soft coating I by a multilayer package requires a much larger number of layer partitions than hard coating II with the same contrast $|\log \gamma|$. The computing expenditures required for achieving the given accuracy $\varepsilon = 0.01$ within the gradient (solid line) and multilayer (dotted line) models is shown in Fig. 3d as a function of γ ; the calculation time at the ordinate axis is normalized to the time of solving the problem for 100 layers. As expected, the multilayer model as a whole is less time-consuming. However, at a high contrast of the soft coating ($\gamma < 1$), the number of layers required for good approximation and the computing expenditure sharply increase, while the expenditure curve for the gradient model remains gently sloping and its use becomes more advantageous for γ lower than a certain threshold value γ^* . The high efficiency of the gradient model is explained by the fact that the derivatives λ' and μ' entering the right-hand part of Eqs. (25) provide better approximation of a high gradient ODE solution than its approximation by a set of solutions for homogeneous layers, in which $\lambda' = \mu' = 0$.

On the other hand, in the course of the comparisons it turned out that even the initial two- and three-layer models without diffusion interlayers ($h_g = 0$) already give an idea about the effect of the corresponding gradient coating on the SAW characteristics. The transformation of the SAW characteristics upon the gradient zone variation is discussed in detail in the following section.

SURFACE WAVES

The presence of the coating leads to a change in the fundamental Rayleigh mode characteristics and to the appearance of additional traveling waves. Some general regularities are maintained for any type of inhomogeneity. At low frequencies ($\omega \rightarrow 0$), when the relative thickness $H/\lambda_s \rightarrow 0$ ($\lambda_s = v_s/f$ is the length of the S -wave in the hard material), the effect of the coating reduces to zero and a single Rayleigh wave propa-

gates in the medium with the same velocity v_R , as in the homogeneous half-space with the properties of the substrate. Therefore, in all plots depicting the slowness s_n versus ω , the first branch of the dispersion curves originates at $\omega = 0$ from the point $s_{R2} = 1/v_R$ (for the hard substrate $s_{R2} = 1.09$; for the soft one $s_{R2} = 2.23$). At the other end of the frequency range $H/\lambda_s \rightarrow \infty$ as $\omega \rightarrow \infty$, and the properties of the upper part of the coating become dominate. Therefore, at high ω , the slowness of all SAWs tends to s_{R1} for the Rayleigh wave in the half-space with the same properties as at $z = 0$.

If the SAW velocity exceeds the S -wave velocity v_s in the substrate, then its propagation excites body waves causing the energy outflow into the lower half-space. The traveling wave is turned into a leaky or pseudosurface wave (PSAW) with the complex wave-number ζ_n , causing its exponential decay with distance in accordance with Eq. (12),

$$|\mathbf{u}_n| \sim ce^{-|\text{Im}\zeta_n|r} / \sqrt{|\zeta_n|r}, \quad |\zeta_n|r \rightarrow \infty.$$

Accordingly, the poles s_n , located in the band $0 < \text{Res} < 1/v_s$ of the complex plane s , are complex with a positive imaginary part.

In the case of media with finite thickness (layer, package of layers), the elements of the matrix $K(\alpha)$ are meromorphic functions without branching points. Their complex poles are located symmetrically in all four quadrants of the complex plane: $\pm\zeta_n$ and the complex-conjugate $\pm\bar{\zeta}_n$. In the considered case, the branching points κ_j of radicals $\sigma_j = \sqrt{\alpha^2 - \kappa_j^2}$, $j = 1, 2$ for the lower half-space remain unremovable; therefore, $K(\alpha)$ is determined on a Riemann manifold. The choice of the branches of the radicals σ_j in accordance with the radiation condition for the body waves in the lower half-space explicitly determines the sole (physical) Riemann sheet, which is fixed by vertical cuts $\alpha = \pm(\kappa_j + it)$, $0 \leq t < \infty$. Usually, only one of each pair of complex-conjugate poles can be on the physical sheet and contribute to representations (11) and (12). The real poles also have counterparts on the non-physical sheet. When the frequency is varied, the poles move in the complex plane, going off the physical sheet into the nonphysical one when crossing the cuts, or coming back when moving in the opposite direction. The character of the pole motion $s_n(\omega)$ (the form of the dispersion curves) is determined by the coating properties. The figures below depict the positive branches of the real curves or the positive real and imaginary parts of the complex curves ones.

The real branches of the dispersion curves $s_n(\omega)$ for four gradient types of soft coating I ($h_g = 0, 0.5, 0.75$, and 1) are shown in Fig. 4, illustrating the effect of the diffusion layer thickness. The higher modes ($n \geq 2$) appear at the cutoff frequencies ω_n from the level

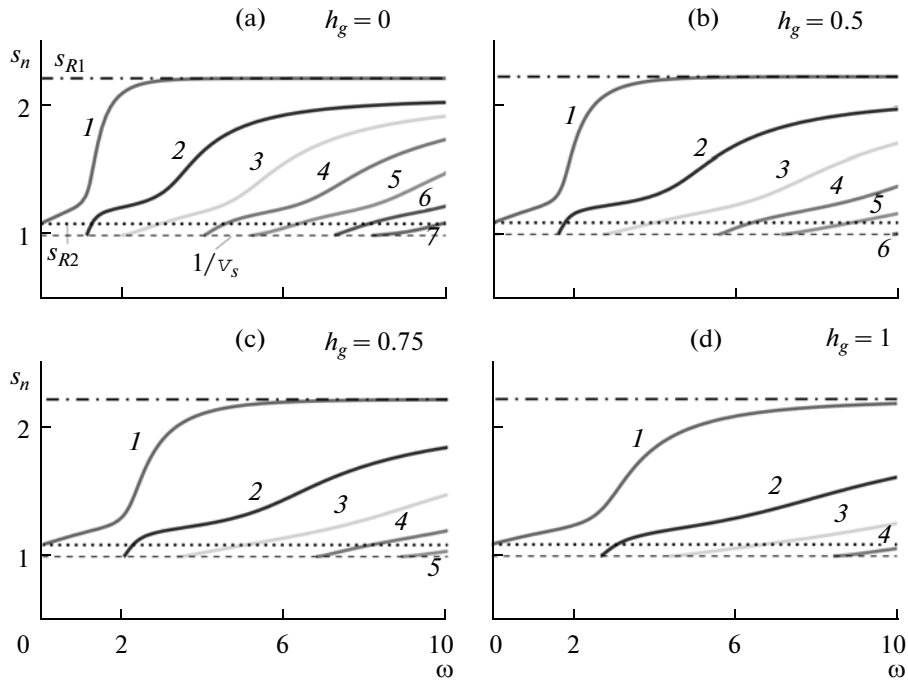


Fig. 4. Real branches of the slowness curves $s_n(\omega)$ for four variants of gradient dependencies in the coating I .

$s^* = 1/v_s = 1$. The complex branches s_n for $\text{Re}s_n < s^*$ are not shown here. As h_g increases, the coating becomes harder and the cutoff frequencies shift to the right, but, in all cases, the s_n values monotonically increase within the range $1 \leq s_n < 2.23$.

The amplitudes $|\mathbf{u}_n|$ at $z = 0$ for the waves excited in the same media I by the concentrated source $\mathbf{q} = \delta\mathbf{i}_3$ (here and below, the amplitudes $|\mathbf{u}_n|$ are calculated at a distance of ten characteristic wavelengths from the source: $r = 10\lambda_s$) are shown in Fig. 5. Their distinguishing feature is that the amplitude of the first mode dominates and increases with frequency, as does the Rayleigh wave amplitude in the homogeneous half-space with the soft material properties (Fig. 5, dash-dotted line). The higher-mode amplitudes, on the contrary, have local maxima only in certain frequency ranges located after the cut-off frequency of the next mode. Every higher mode passes on the maximal amplitude level to the next one, which is clearly seen in Fig. 5a.

For the hard coating II , the first branch of the dispersion curves starts from the value $s_{R2} = 2.23$ and goes downward, quickly crossing the level $s^* = 2.08$ and becoming complex (Fig. 6); here and below $\text{Re}s_n$ and $\text{Im}s_n$ of the complex curves are shown by dashed lines. The pole s_1 goes off into the nonphysical sheet, but in exchange for it, the complex pole s_2 comes to the physical sheet through the boundary specified by the cut, beginning the complex branch of the second

mode. The following poles appear already in the complex-valued zone $\text{Re}s_n < s^*$. With an increase in ω they are either stabilized at some distance from the real axis, just like for the second mode in Figs. 6a and 6b, or approach it, giving PSAWs with very small damping decrements and the slownesses $\text{Re}s_n \approx s_{R1} = 1.09$ (the same as in the half-space with the properties of the hard coating). The latter is typical for the third mode at $h_g \leq 0.5$ (Figs. 6a and 6b) and for the second mode at $h_g \geq 0.75$ (Figs. 6c and 6d). Thus, in a medium with hard coating II , one traveling wave is always excited in the low frequency band $0 < \omega < 0.4$ and one weakly decaying PSAW at $\omega > 10$. The intermediate frequency range is the blocking range that is clearly seen in the plots of PSAW amplitudes (Fig. 7). Here, it is interesting to note the change of the second and third mode contributions into PSAWs with the increase of h_g ;

they exchange with their roles at $h_g = h_g^* = 0.686$, when, at the definite frequency $\omega^* = 7.351$, the complex branches s_2 and s_3 cross, merging in a twofold pole and then diverging apart again at $\omega > \omega^*$ (Fig. 8); the complex poles are numbered according to the rule $\text{Re}s_{n+1} < \text{Re}s_n$.

The distinguishing feature of coatings III and IV is the change of sign of the property gradient with depth; therefore, in different frequency ranges, they reveal properties of both medium I and medium II . Medium III with a hard interlayer resembles medium II because its soft substrate is covered with a

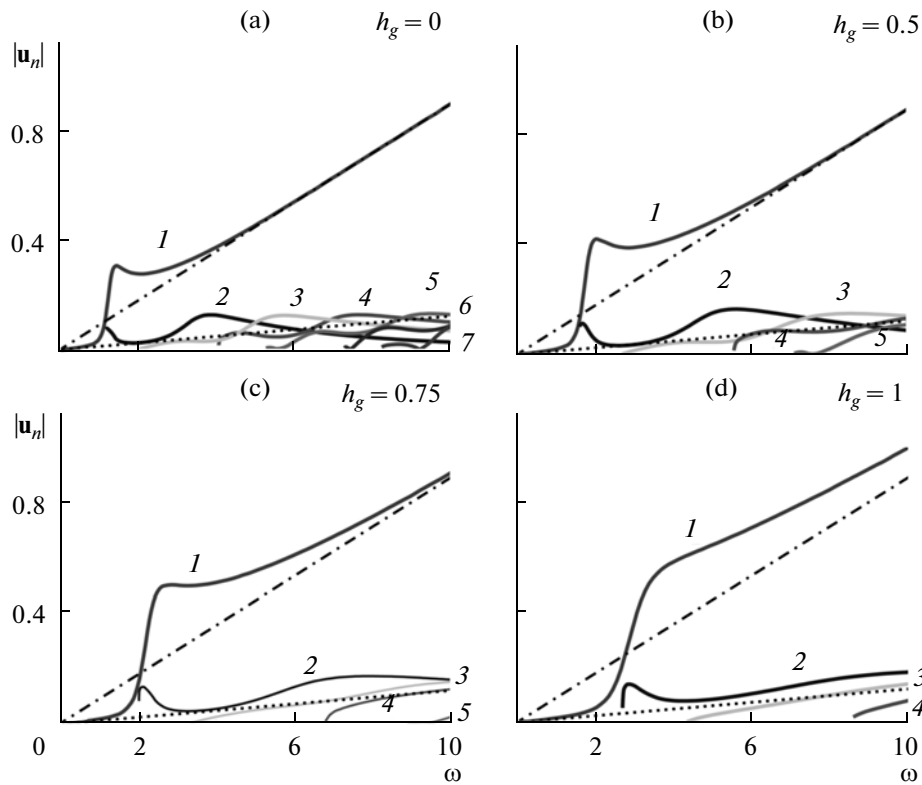


Fig. 5. Amplitudes of the modes u_n excited by the vertical point load; here and below, the dash-dotted and dotted lines are for the Rayleigh wave amplitude u_R in the homogeneous half-spaces with the soft and hard material properties, respectively.

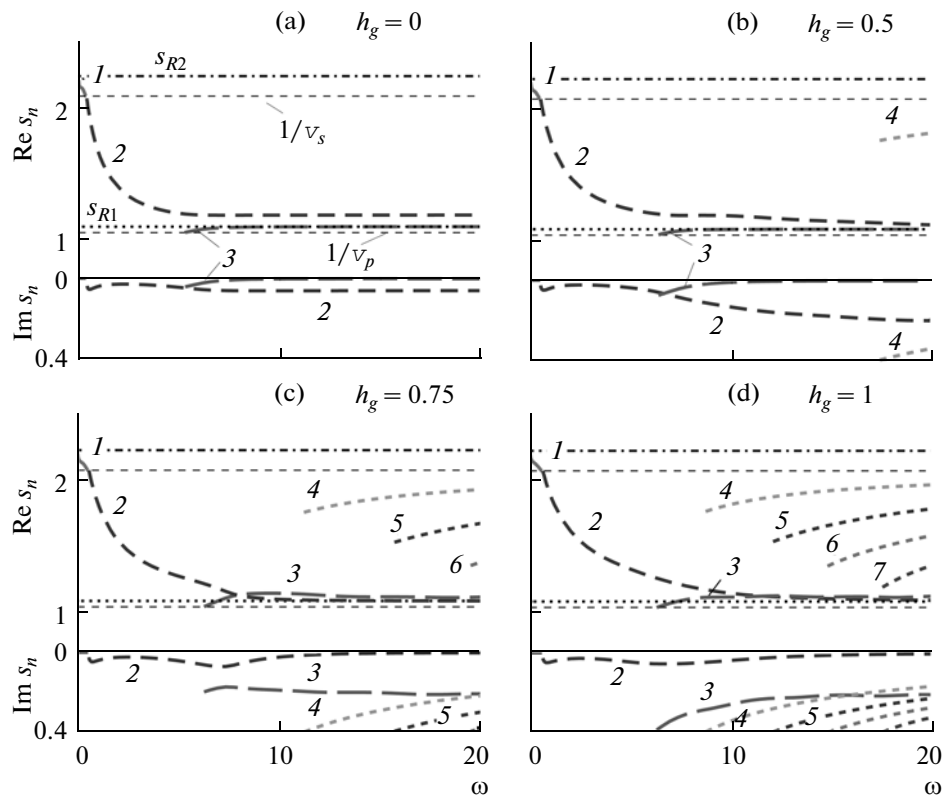


Fig. 6. Low-frequency region of the real-valued section of $s_1(\omega)$ and complex branches of the higher modes for different variants of hard coating II.

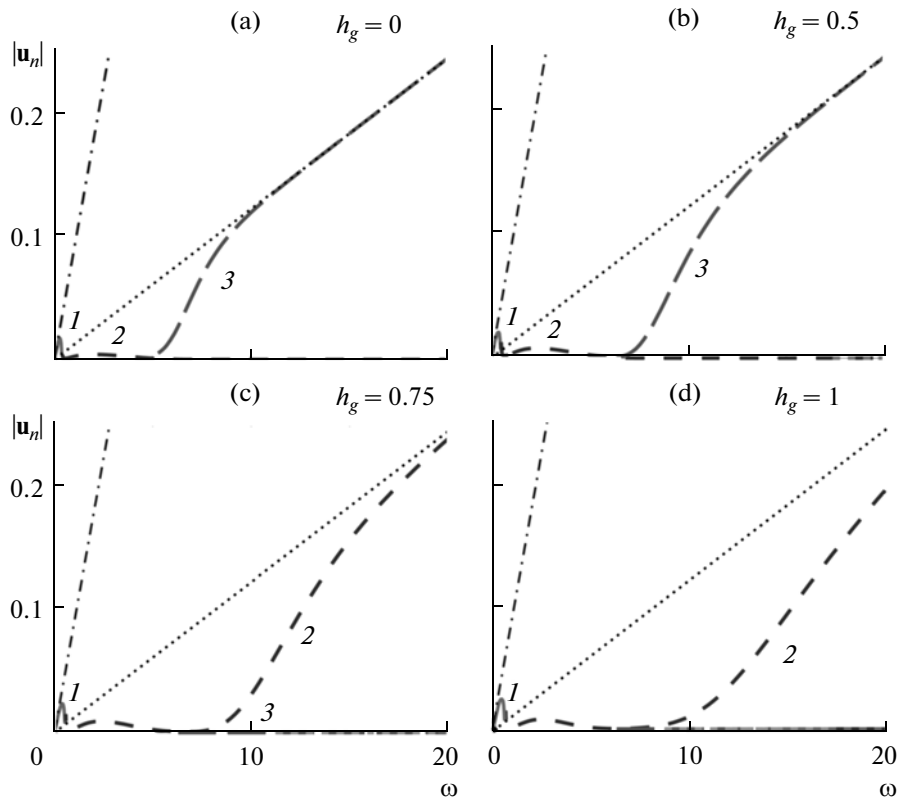


Fig. 7. SAW and PSAW amplitudes at the distance $r = 10\lambda_s$ from the source, coating II.

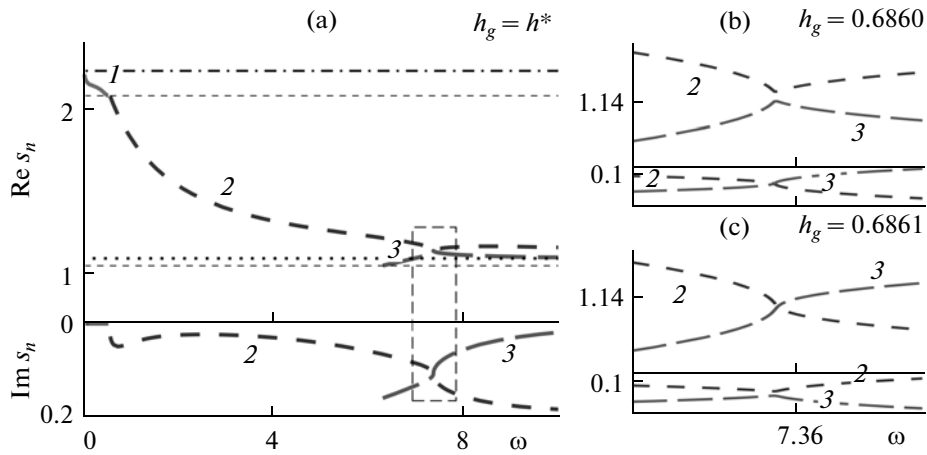


Fig. 8. Effect of the complex pole merging into the twofold pole in the case of hard coating II.

harder layer. The curve $s_1(\omega)$ here is also quickly lowered to the branch point s^* and goes out into the non-physical sheet, while the complex branch $s_2(\omega)$ appears in its place (Fig. 9). However, starting from a certain frequency, due to the presence of the upper soft layer, traveling wave can be excited in this medium once again. This is revealed in the complex pole s_2 coming up into the real-valued zone. However, unlike

medium I, the rest of the branches remain complex, although some of them almost touch the real axis, giving PSAWs with very small attenuation (see, for example, branch s_3 at $h_g = 0$).

In more detail, the replacement of the curve $s_1(\omega)$ by $s_2(\omega)$ occurs as follows. When the real pole s_1 moves to the branch point $s^* = 2.08$ with the increase of ω ,

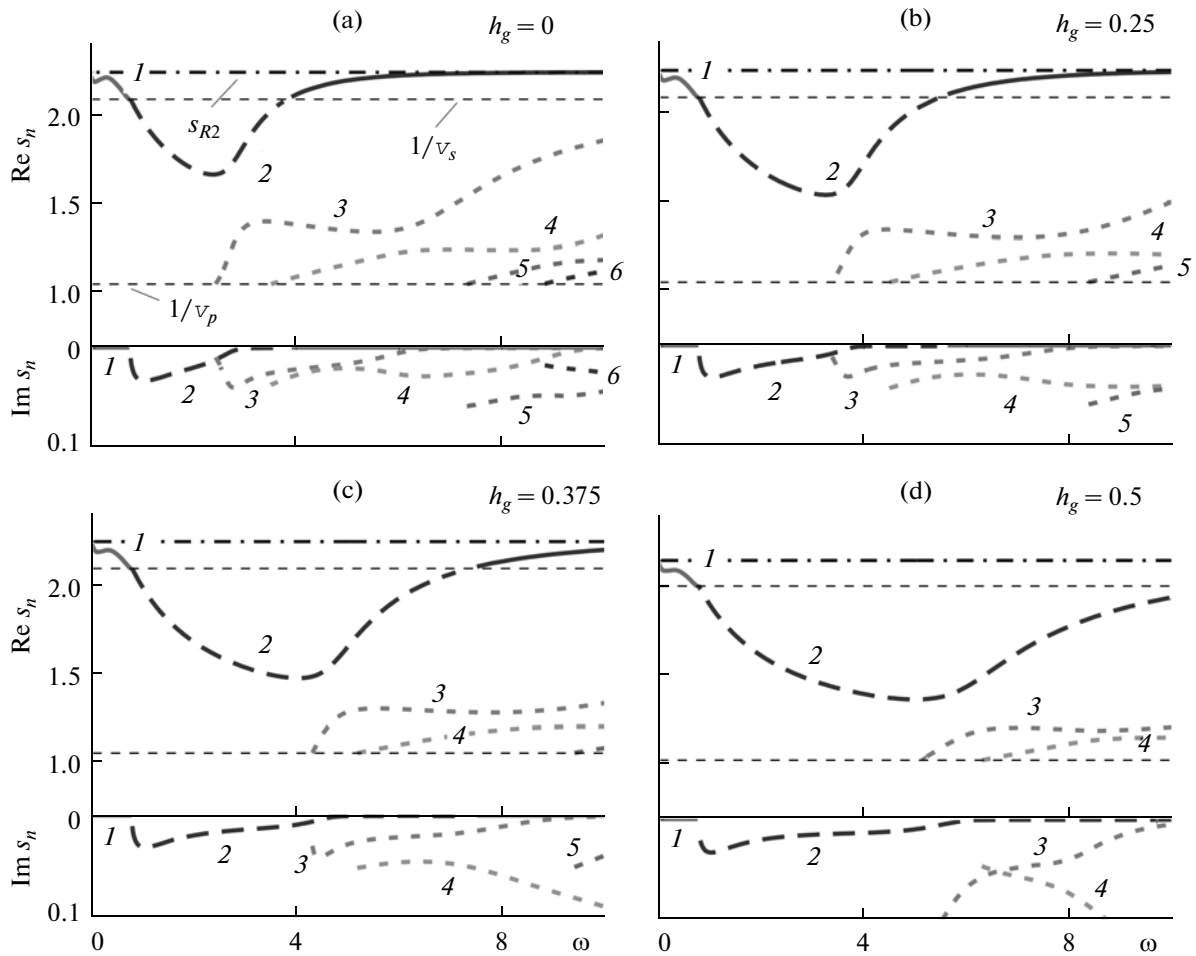


Fig. 9. Slowness curves for different types of coating III.

the counterpart pole \tilde{s}_2 located in the nonphysical sheet also moves to s^* , somewhat staying behind s_1 . At $\omega = 0.77$ ($h_g = 0.25$), the pole s_1 passes the branch point and goes out into the nonphysical sheet, moving along the real axis toward \tilde{s}_2 . Then they merge in the twofold pole and diverge into the lower and upper half-planes as a pair of complex-conjugate poles \tilde{s}_1 and \tilde{s}_2 . Then, at $\omega = 0.80$, the pole \tilde{s}_2 crosses the cut, coming into the physical sheet as a complex branch $s_2(\omega)$, while \tilde{s}_1 moves not intersecting the cut and remaining in the nonphysical sheet. Note that, in the range of $0.77 < \omega < 0.80$, both poles are in the nonphysical sheet and do not contribute to Eqs. (11) and (12). Instead, the contribution of the integral over the cut banks, which describes the body waves, strongly increases; i.e., a phenomenon of wave energy reradiation into the lower half-space takes place here, because the energy is carried down by the body waves.

At $\omega = 5.45$, the complex poles s_2 and \tilde{s}_1 return to the branch point s^* , leaving then to the real axes of the physical and nonphysical sheet, respectively. The fre-

quency range remains in the blocking mode from the departure of s_1 to the nonphysical sheet until the return of s_2 . At the beginning of this range, already at the distance $r = 10\lambda_s$ from the source, the wave field amplitude on the surface $z = 0$ is almost zero (Fig. 10). Then, it once again increases due to the contribution of the second mode, the complex pole s_2 of which approaches the real axis. After its return to the real axis, its contribution to the wave-field amplitude becomes dominant, just like in medium I.

The medium with coating IV is a typical example of waveguides with an internal sound channel [16]. A set of traveling waves propagates in it (Fig. 11), similarly to the SAW set in the medium with coating I (see Fig. 5). The thickness of gradient interlayers less affects their properties than in other cases; therefore, Figs. 11 and 12 give examples only for two limiting values $h_g = 0$ and $h_g = 0.5$. The main difference from the medium I is observed in the behavior of the fundamental mode s_1 . First, the dependence of s_1 on ω becomes nonmonotonic: a descending part of the

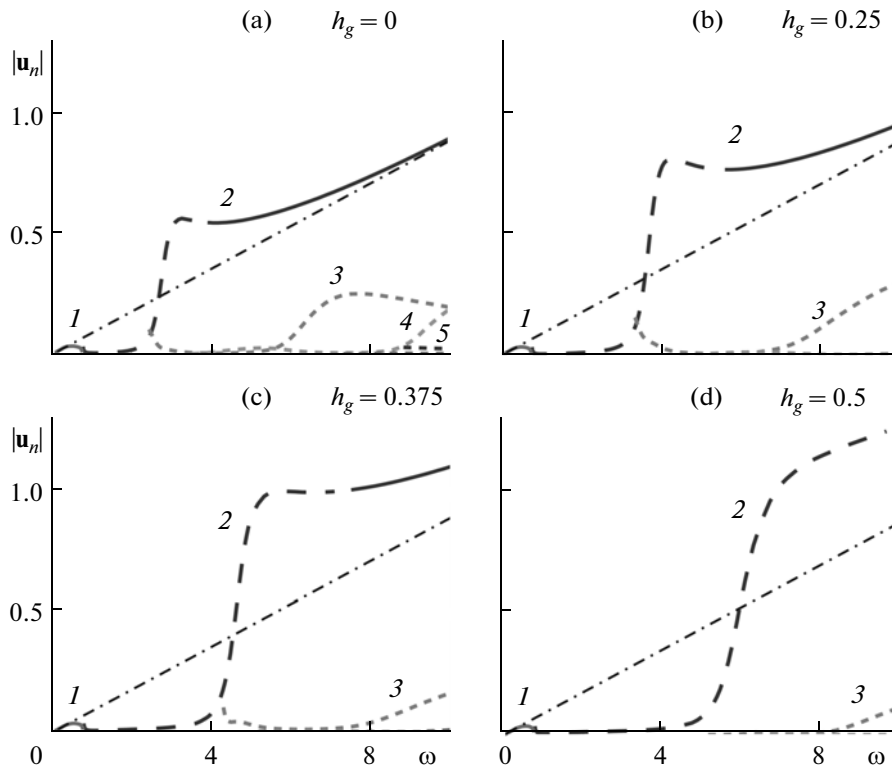


Fig. 10. Amplitudes of the corresponding modes in medium III.

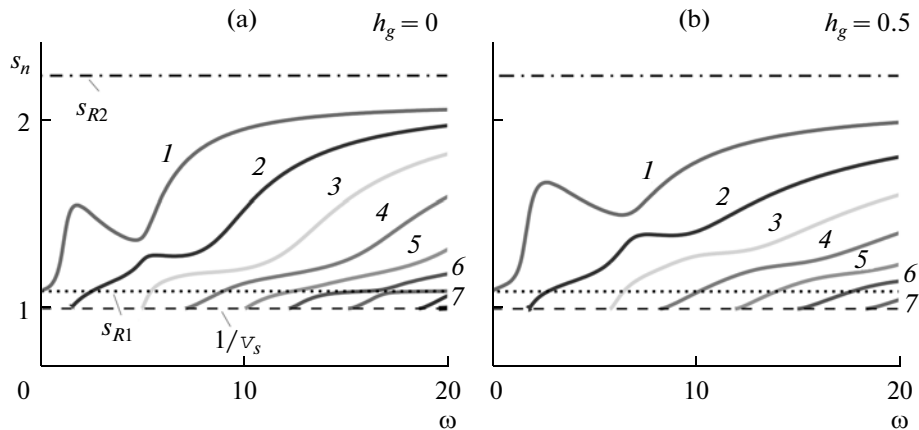


Fig. 11. Real branches of the dispersion curves for piecewise-uniform (a) and gradient over the whole thickness (b) of coating IV.

curve s_1 appears. Second, its amplitude is no longer dominant and, as in other modes, it makes the main contribution to the wave field only in a limited frequency range (Fig. 12). Here, as in medium I, the dominance of the amplitude is passed on from one mode to another as ω increases. The continuous change in the form of slowness and amplitude curves for the first three modes in the course of gradual variation of the diffusion layer thickness h_g in coating IV is illustrated in Fig. 13.

CONCLUSIONS

Efficient methods of analyzing wave fields excited by a surface load in an elastic half-space with continuous depth dependence of the properties have been elaborated and implemented. The influence of the properties of inhomogeneous coatings on the acoustic wave characteristics has been analyzed.

Systematic comparison of the results obtained within the gradient and multilayer models confirms the possibility to approximate the FGM properties by

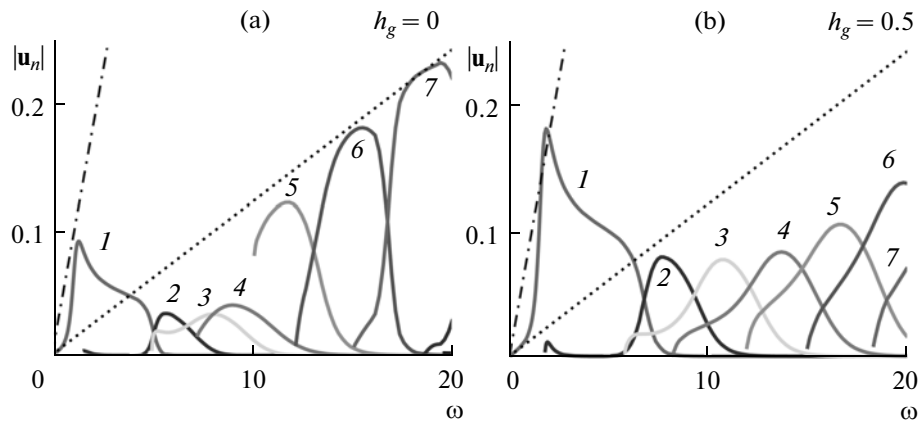


Fig. 12. Amplitudes of the corresponding modes in medium IV.

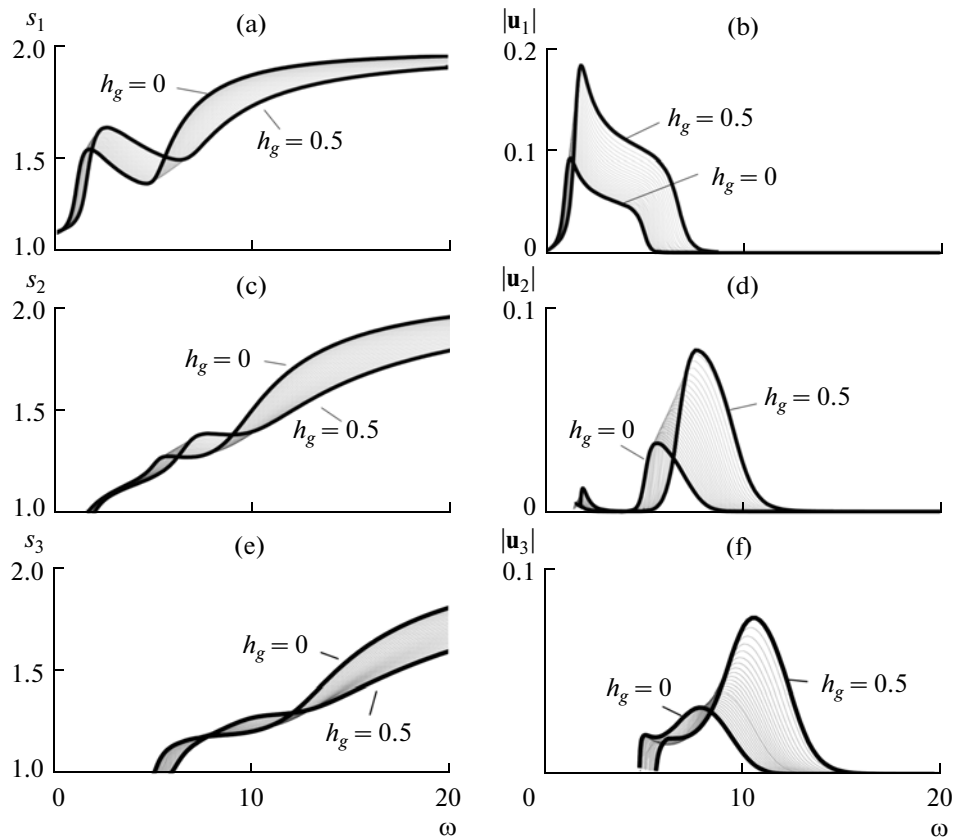


Fig. 13. Dispersion curves and amplitudes of the first three modes upon smooth change of the gradient interlayer thickness h_g in coating IV.

steplike dependences for wave process simulation on the day surface. For a soft coating with strongly contrast properties, such an approximation makes no sense, since it leads to higher computing costs than those in the initial gradient model.

ACKNOWLEDGMENTS

This work was supported by the German Research Society DFG (ZH 15/16-1) and the Russian Foundation for Basic Research (project no. 11-01-96509).

REFERENCES

1. E. Moulin, J. Assaad, C. Delebarre, and D. Osmont, *J. Acoust. Soc. Am.* **107**, 87 (2000).
2. I. I. Vorovich and V. A. Babeshko, *Mixed Dynamic Problems of the Theory of Elasticity for Nonclassical Domains* (Nauka, Moscow, 1979) [in Russian].
3. I. V. Anan'ev and V. A. Babeshko, *Mekh. Tverd. Tela*, No. 1, 64 (1978) [in Russian].
4. N. V. Glushkova, Candidate's Dissertation in Physics and Mathematics (Rostov. State Univ., Rostov-on-Don, 1981) [in Russian].
5. S. M. Aizikovich, V. M. Aleksandrov, A. V. Belokon', L. I. Krenev, and I. S. Trubchik, *Contact Problems of the Theory of Elasticity for Inhomogeneous Media* (Fizmatlit, Moscow, 2006) [in Russian].
6. V. V. Kalinchuk and T. I. Belyankova, *The Dynamics of the Surface of Inhomogeneous Media* (Fizmatlit, Moscow, 2009) [in Russian].
7. V. A. Babeshko, E. V. Glushkov, and N. V. Glushkova, *Zh. Vychisl. Mat. Mat. Fiz.* **27**, 93 (1987).
8. W. T. Thomson, *J. Appl. Phys.* **21**, 89 (1950).
9. N. A. Haskell, *Bull. Seism. Soc. Am.* **43**, 17 (1953).
10. G. I. Petrashen', *Uch. Zap. LGU* **162**, 3 (1952) [in Russian].
11. O. Matsuda and C. Glorieux, *J. Acoust. Soc. Am.* **121**, 3437 (2007).
12. V. A. Babeshko, E. V. Glushkov, and Zh. F. Zinchenko, *Dynamics of Inhomogeneous Linearly Elastic Media* (Nauka, Moscow, 1989), p. 344 [in Russian].
13. H. Schmidt and G. Tango, *Geophys. J. R. Astron. Soc.* **84**, 331 (1986).
14. E. V. Glushkov, N. V. Glushkova, and S. I. Fomenko, *Acoust. Phys.* **57**, 230 (2011).
15. E. Glushkov, N. Glushkova, and A. Eremin, *J. Acoust. Soc. Am.* **129**, 2923 (2011).
16. L. M. Brekhovskikh, *Waves in Layered Media* (Nauka, Moscow, 1973; Academic, New York, 1980).